

The electromagnetic form factors of the Ω^- in lattice QCD

C. Alexandrou^(a,b), T. Korzec^(c), G. Koutsou^(d,e), J. W. Negele^(f), Y. Proestos^(b)

^(a) *Department of Physics, University of Cyprus,
P.O. Box 20537, 1678 Nicosia, Cyprus*

^(b) *Computation-based Science and Technology Research Center,
The Cyprus Institute, P.O. Box 27456,
1645 Nicosia, Cyprus*

^(c) *Humboldt Universität zu Berlin,
Newtonstrasse 15, 12489 Berlin, Germany*

^(d) *Jülich Supercomputing Center,
Forschungszentrum Jülich, D-52425 Jülich, Germany*

^(e) *Bergische Universität Wuppertal,
Gaussstr. 20, D-42119 Wuppertal, Germany*

^(f) *Center for Theoretical Physics,
Laboratory for Nuclear Science and Department of Physics,
Massachusetts Institute of Technology,
Cambridge, Massachusetts 02139, U.S.A.*

We present results on the Omega baryon (Ω^-) electromagnetic form factors using $N_f = 2 + 1$ domain-wall fermion configurations for three pion masses in the range of about 350 to 300 MeV. We compare results obtained using domain wall fermions with those of a mixed-action (hybrid) approach, which combines domain wall valence quarks on staggered sea quarks, for a pion mass of about 350 MeV. We pay particular attention in the evaluation of the subdominant electric quadrupole form factor to sufficient accuracy to exclude a zero value, by constructing a sequential source that isolates it from the dominant form factors. The Ω^- magnetic moment, μ_{Ω^-} , the electric charge and magnetic radius, $\langle r_{E0/M1}^2 \rangle$, are extracted for these pion masses. The electric quadrupole moment is determined for the first time using dynamical quarks.

PACS numbers: 11.15.Ha, 12.38.Gc, 12.38.Aw, 12.38.-t, 14.70.Dj

I. INTRODUCTION

The structure of hadrons, such as size, shape and charge distribution can be probed by their electromagnetic form factors. The Ω^- baryon, consisting of three valence strange quarks is, significantly more stable than other members of the baryon decuplet, such as the Δ , with a life-time of the order of 10^{-10} s. This fact makes the calculation of its electromagnetic form factors particularly interesting since they are accessible to experimental measurements with smaller theoretical uncertainties. Its magnetic dipole moment is measured to very good accuracy, unlike those of the other decuplet baryons. A value of $\mu_{\Omega^-} = -2.02(5)$ is given in the PDG [1] in units of nuclear magnetons (μ_N). Within lattice QCD one can directly compute hadron form factors starting from the fundamental theory of the strong interactions. Furthermore, higher order multipole moments, not detectable by current experimental setups, are accessible to lattice methods and can reveal important information on the structure of the hadron. An example is the electric quadrupole moment, which detects deformation of a hadron state.

In this work we calculate, for the first time, the electromagnetic form factors of the Ω^- baryon using dynamical domain-wall fermion configurations. For the calculation we use the fixed-sink approach, which enables the calculation of the form factors for all values and directions of the momentum transfer \vec{q} concurrently. The main advantage of this approach is that it allows an increased statistical precision, while at the same time it provides the full Q^2 dependence, where $Q^2 = -q^2$. In order to obtain accurate results on the form factors we construct optimized sources for the sequential inversion. This is particularly important for the subdominant electric quadrupole form factor, for which we construct an appropriate source that isolates it from the two dominant form factors [2]. This requires extra sequential inversions but it is essential in order to determine the electric quadrupole form factor to good accuracy.

The form factors are calculated using $N_f = 2 + 1$ dynamical domain-wall fermion configurations at the three lowest pion masses currently available, namely $m_\pi = 350$ MeV, $m_\pi = 330$ MeV and $m_\pi = 297$ MeV. The results are compared to those obtained with a hybrid action that uses domain wall valence quarks on staggered sea quarks simulated by the MILC collaboration [3].

The paper is organized as follows: In Section II we provide the definitions of the corresponding multipole form factors and describe the lattice setup to extract them. In Section III we discuss the results and in Section IV we give the conclusions.

II. LATTICE TECHNIQUES

A. Electromagnetic matrix element

The Ω^- has spin and isospin $3/2$ and therefore the decomposition of the electromagnetic matrix element is the same as that of the Δ . The on-shell Ω^- matrix element of the electromagnetic current V^μ , is decomposed in terms of four independent Lorentz covariant vertex functions, $a_1(q^2)$, $a_2(q^2)$, $c_1(q^2)$ and $c_2(q^2)$, which depend only on the squared momentum transfer $q^2 = -Q^2 = (p_i - p_f)^2$. The initial and final four-momentum are given by p_i and p_f , respectively. In Minkowski spacetime these covariant vertex functions are given by [4]

$$\langle \Omega(p_f, s_f) | V^\mu | \Omega(p_i, s_i) \rangle = \sqrt{\frac{m_\Omega^2}{E_\Omega(p_f) E_\Omega(p_i)}} \bar{u}_\sigma(p_f, s_f) \mathcal{O}^{\sigma\mu\tau} u_\tau(p_i, s_i), \quad (1)$$

$$\mathcal{O}^{\sigma\mu\tau} = -g^{\sigma\tau} \left[a_1(q^2) \gamma^\mu + \frac{a_2(q^2)}{2m_\Omega} (p_f^\mu + p_i^\mu) \right] - \frac{q^\sigma q^\tau}{4m_\Omega^2} \left[c_1(q^2) \gamma^\mu + \frac{c_2(q^2)}{2m_\Omega} (p_f^\mu + p_i^\mu) \right]. \quad (2)$$

The rest mass and the energy of the particle are denoted by m_Ω and E_Ω , respectively. The initial and final spin-projections are given by s_i and s_f , respectively. Recall also that every vector component of the spin- $\frac{3}{2}$ Rarita-Schwinger vector-spinor u_σ satisfies the Dirac equation, $(p_\mu \gamma^\mu - m_\Omega) u^\sigma(p, s) = 0$, along with the auxiliary conditions: $\gamma_\sigma u^\sigma(p, s) = 0$ and $p_\sigma u^\sigma(p, s) = 0$. Additionally, the covariant vertex functions are linearly related to the (dimensionless) electric $G_{E0}(q^2)$, $G_{E2}(q^2)$ and magnetic $G_{M1}(q^2)$, $G_{M3}(q^2)$ multipole form factors [2, 4]. Namely, the expressions relating the multipole form factors and the covariant vertex functions are given in Ref. [4] and are quoted below for reference:

$$G_{E0} = (1 + \frac{2}{3}\tau)[a_1 + (1 + \tau)a_2] - \frac{1}{3}\tau(1 + \tau)[c_1 + (1 + \tau)c_2], \quad (3)$$

$$G_{E2} = a_1 + (1 + \tau)a_2 - \frac{1}{2}(1 + \tau)[c_1 + (1 + \tau)c_2], \quad (4)$$

$$G_{M1} = (1 + \frac{4}{5}\tau)a_1 - \frac{2}{5}\tau(1 + \tau)c_1, \quad (5)$$

$$G_{M3} = a_1 - \frac{1}{2}(1 + \tau)c_1, \quad (6)$$

$$(7)$$

where the positive quantity $\tau = -\frac{q^2}{4m_\Omega^2}$.

B. Lattice setup

We use gauge configurations generated by the RBC-UKQCD collaborations using $N_f = 2 + 1$ domain-wall fermions [5] and the Iwasaki gauge-action. The simulations are carried out on two lattices of size $24^3 \times 64$ at a pion mass of 330 MeV and $32^3 \times 64$ at pion masses of 355 MeV and 297 MeV, respectively. The latter has a smaller lattice spacing and therefore we will refer to it as the fine lattice. For the $24^3 \times 64$ lattice, or coarse lattice, the lattice spacing a , the light u- and d-quark mass as well as the strange quark mass were fixed by an iterative procedure using the Ω^- , the pion and the kaon masses [5] as inputs. The value obtained for the lattice spacing is $a^{-1} = 1.729(28)$ GeV [5]. For the fine lattice the scale was fixed from the ratio of the pion decay constant, f_π calculated on the fine lattice to the one computed on the $24^3 \times 64$ at the same values of the ratio m_π/f_π . The value found is $a^{-1} = 2.34(3)$ GeV [6]. In addition, to these two lattices, we perform the calculation using a mixed-action with domain-wall valence quarks and staggered sea quarks. The gauge configurations were produced by the MILC collaboration [7, 8] using two degenerate flavors of light staggered sea quarks and a strange staggered sea quark fixed to its physical mass. The lattice size is $28^3 \times 64$ and the mass of the light quarks corresponds to a pion mass of 353 MeV. The lattice spacing is 0.124 fm as determined from the $\Upsilon' - \Upsilon$ mass difference [7]. For the valence quarks we use domain wall fermions (DWF). The valence strange-quark mass was set using the $N_F = 3$ ensemble by requiring the valence pseudoscalar mass to be equal to the mass of the Goldstone boson constructed using staggered quarks [9]. Similarly the light quark valence mass is tuned by adjusting the DWF pion mass to the taste-5 staggered Goldstone boson pion. The domain wall quark masses take the values given in Table I. Technical details of this tuning procedure are given in Refs. [9–11].

In all cases we used $N_5 = 16$, which is what was used in the simulation of the dynamical domain wall fermions. We note that for the coarse lattice at the pion mass used here the residual mass is large compared to the bare quark mass

and chiral symmetry breaking is expected. The value of $N_5 = 16$ is also used in the mixed action calculation where it was shown that the residual mass is 10% of the bare quark mass, ensuring small chiral symmetry breaking [10]. In Table I we provide details of the simulations, along with the value of the mass of the Ω^- obtained in this work as well as the value computed by other groups when available.

$L_s^3 \times L_T$	$N_{\text{confs}}^{\text{subd.}}$	$N_{\text{confs}}^{\text{dom.}}$	a^{-1} [GeV]	$m_{u,d}/m_s$	m_π [GeV]	m_N [GeV]	m_Ω [GeV]
$N_F = 2 + 1$ domain wall fermions [5]							
$24^3 \times 64$	200	200	1.729(28)	0.005/0.04	0.329(1)	1.154(7) [12]	1.77(3) (1.758(9)) [5]
$N_F = 2 + 1$ domain wall fermions [6]							
$32^3 \times 64$	–	105	2.34(3)	0.006/0.03	0.355(6)	1.172(21)	1.79(4)
$32^3 \times 64$	200	120	2.34(3)	0.004/0.03	0.297(5)	1.109(21)	1.76(2)
Mixed action [18]							
DWF valence: $am_{u,d} = 0.0138$, $am_s = 0.081$							
$28^3 \times 64$	210	120	1.58(3)	0.01/0.05	0.353(2)	1.191(19)	1.78(3) (1.775(5)) [9]

TABLE I: Parameters used in the calculation of the form factors. We give the number of configurations $N_{\text{confs}}^{\text{subd.}}$ used to extract the subdominant electric quadrupole form factor G_{E2} , as well as the number of configurations used $N_{\text{confs}}^{\text{dom.}}$ to extract the dominant form factors for the various lattices employed in this study. The Ω^- hyperon mass as determined in this work is given in the last column and it is compared with the value determined by the RBC-UKQCD collaboration and the LHPC for the mixed action as given in parenthesis.

C. Interpolating fields

In order to calculate the on-shell matrix element we utilize appropriate two- and three-point correlation functions. An interpolating field operator with the quantum numbers of the Ω^- baryon is given by

$$\chi_{\sigma\alpha}(x) = \epsilon^{abc} \mathbf{s}_\alpha^a (\mathbf{s}_\beta^{tb} [C\gamma_\sigma]_{\beta\gamma} \mathbf{s}_\gamma^c), \quad (8)$$

where $C = \gamma_4\gamma_2$ is the charge-conjugation matrix and σ represents the vector index of the spin- $\frac{3}{2}$ spinor. To ensure ground state dominance at the shortest possible Euclidean time separation we perform a gauge invariant Gaussian smearing on the strange quark fields that enter in the interpolating field, as described in Refs. [13, 14]:

$$\mathbf{s}_\beta(t, \vec{x}) = \sum_{\vec{y}} [1 + \alpha H(\vec{x}, \vec{y}; U)]^{n_W} \mathbf{s}_\beta(t, \vec{y}), \quad (9)$$

$$H(\vec{x}, \vec{y}; U) = \sum_{\mu=1}^3 (U_\mu(\vec{x}, t) \delta_{\vec{x}, \vec{y}-\hat{\mu}} + U_\mu^\dagger(\vec{x}-\hat{\mu}, t) \delta_{\vec{x}, \vec{y}+\hat{\mu}}), \quad (10)$$

where \mathbf{s} is the smeared s-quark field. The links $U_\mu(\vec{x}, t)$ entering the hopping matrix H are APE-smearing gauge fields. In particular, for DWF on the coarse lattice we have used the Gaussian smearing parameters $\alpha = 5.026$ and $n_W = 40$, while for the fine lattice the corresponding smearing parameters are $\alpha = 7.284$ and $n_W = 84$. These are the same parameters as those used to ensure optimal filtering of the nucleon state [6].

In Fig. 1 we show the results for the Ω^- effective mass calculated from the two-point function ratio $am_{\text{eff}}^{\Omega^-}(t) = -\log[G(t+1, \vec{0})/G(t, \vec{0})]$ for the three different sets of configurations considered in this study, The results are summarized in Table I.

For the DWF simulations, on both the coarse and fine lattices considered in this work, the resulting values for the Ω^- mass are 1.77(3) GeV and 1.76(2) GeV, respectively. These values agree with the value found in Ref. [5]. The same agreement is obtained in the case of the hybrid action. In Ref. [5] it was found that, at the chiral limit, the Ω^- mass decreases by about 2% its value at $am_{u,d} = 0.005$. Compared to the experimental value of 1.672 GeV [1] the value obtained at the physical point is about 50 MeV higher indicating that the strange quark mass is a few percent larger than the physical one in these simulations.

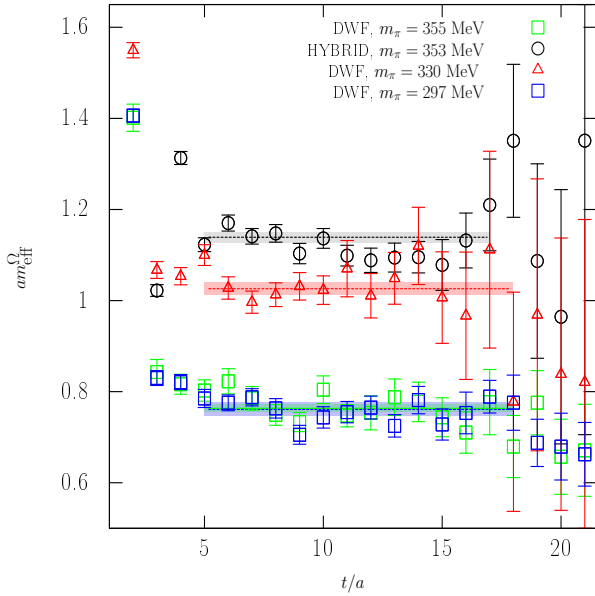


FIG. 1: The Ω^- effective mass and the fit to a constant plotted against the time separation for each ensemble considered. The statistics used to extract the effective masses are summarized in Table I.

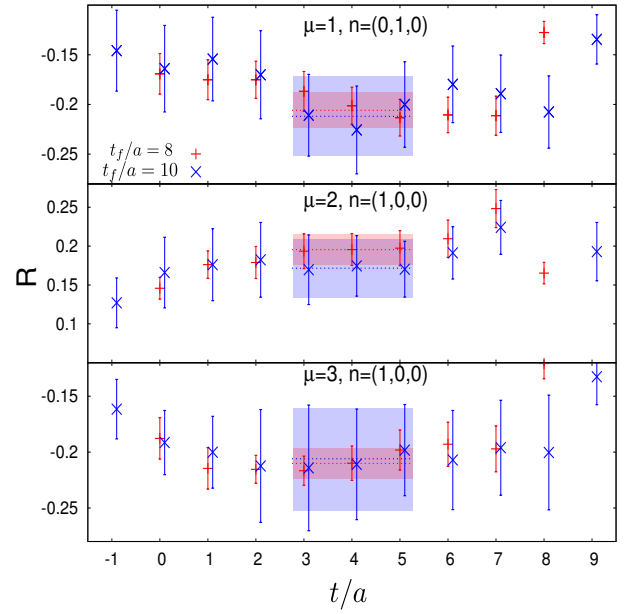


FIG. 2: The ratio $R \equiv R_{\sigma\tau\mu}(\Gamma, \vec{q}, t)$ extracted for temporal source-sink separations $t_f/a = 8$ and $t_f/a = 10$, using 50 gauge configurations. The results for $t_f/a = 10$ are shifted to the left by one unit. We show results for current direction $\mu = 1$ and $\mu = 2, 3$ and momenta \vec{q} : $(0, 1, 0) \frac{2\pi}{L}$ and $(1, 0, 0) \frac{2\pi}{L}$, respectively. The bands correspond to the constant form fit errors.

D. Two- and three-point Correlation functions

The electromagnetic form factors can be extracted in lattice QCD by constructing appropriate combinations of two- and three-point correlation functions. The corresponding lattice correlation functions are given by

$$G_{\sigma\tau}(\Gamma^\nu, \vec{p}, t) = \sum_{\vec{x}_f} e^{-i\vec{x}_f \cdot \vec{p}} \Gamma_{\alpha'\alpha}^\nu \left\langle \chi_{\sigma\alpha}(t, \vec{x}_f) \bar{\chi}_{\tau\alpha'}(0, \vec{0}) \right\rangle, \quad (11)$$

$$G_{\sigma\mu\tau}(\Gamma^\nu, \vec{q}, t) = \sum_{\vec{x}, \vec{x}_f} e^{i\vec{x} \cdot \vec{q}} \Gamma_{\alpha'\alpha}^\nu \left\langle \chi_{\sigma\alpha}(t_f, \vec{x}_f) V_\mu(t, \vec{x}) \bar{\chi}_{\tau\alpha'}(0, \vec{0}) \right\rangle. \quad (12)$$

For our lattice setup we take a frame where the final Ω^- -state is produced at rest i.e. $\vec{p}_f = \vec{0}$. Furthermore lattice calculations are carried out in a Euclidean space-time, and hence from here on all expressions are given with Euclidean conventions [15]. We use the local vector current V_μ carrying a momentum $\vec{q} = -\vec{p}_i$, which is inserted at time t . The renormalization constant Z_V is determined by the condition $G_E(0) = -1$. The Γ matrices are given by

$$\Gamma^4 = \frac{1}{4}(\mathbf{1} + \gamma^4), \quad \Gamma^k = \frac{i}{4}(\mathbf{1} + \gamma^4)\gamma_5\gamma_k, \quad k = 1, 2, 3. \quad (13)$$

By inserting into the correlation functions a complete set of energy momentum eigenstates

$$\sum_{n,p,\xi} \frac{M_n}{V E_n(p)} |n(p, \xi)\rangle \langle n(p, \xi)| = \mathbf{1}, \quad (14)$$

with ξ denoting all other quantum numbers, such as spin, one finds that the leading contributions for large Euclidean times t and $t_f - t$ are

$$G_{\sigma\tau}(\Gamma^\nu, \vec{p}, t) = \frac{M_\Omega}{E_\Omega(p)} |Z|^2 e^{-E_\Omega(p)t} \text{tr} [\Gamma^\nu \Lambda_{\sigma\tau}^E(p)] + \text{excited states}, \quad (15)$$

$$G_{\sigma\mu\tau}(\Gamma^\nu, \vec{q}, t) = \frac{M_\Omega}{E_\Omega(p_i)} |Z|^2 e^{-M_\Omega(t_f-t)} e^{-E_\Omega(p_i)t} \text{tr} [\Gamma^\nu \Lambda_{\sigma\sigma'}^E(p_f) \mathcal{O}_{\sigma'\mu\tau'}^E \Lambda_{\tau'\tau}^E(p_i)] + \text{excited states}. \quad (16)$$

The leading time dependence and unknown overlaps of the Ω^- state with the initial state $\bar{J}_\Omega|0\rangle$ in the three-point correlation function can be canceled out by forming appropriate ratios that involve both the two- and three-point functions. The ratio employed in this work is given by the following expression

$$R_{\sigma\mu\tau}(\Gamma, \vec{q}, t) = \frac{G_{\sigma\mu\tau}(\Gamma^\nu, \vec{q}, t)}{G_{kk}(\Gamma^4, \vec{0}, t_f)} \sqrt{\frac{G_{kk}(\Gamma^4, \vec{p}_i, t_f - t) G_{kk}(\Gamma^4, \vec{0}, t) G_{kk}(\Gamma^4, \vec{0}, t_f)}{G_{kk}(\Gamma^4, \vec{0}, t_f - t) G_{kk}(\Gamma^4, \vec{p}_i, t) G_{kk}(\Gamma^4, \vec{p}_i, t_f)}}, \quad (17)$$

where a summation over the repeated indices k ($k = 1, 2, 3$) is understood. This ratio becomes time-independent (displays a plateau) for large Euclidean time separations, that is

$$R_{\sigma\mu\tau}(\Gamma, \vec{q}, t) \xrightarrow{t_f - t \gg 1, t \gg 1} \Pi_{\sigma\mu\tau}(\Gamma, \vec{q}) = \mathcal{C} \text{Tr} [\Gamma \Lambda_{\sigma\sigma'}(p_f) \mathcal{O}_{\sigma'\mu\tau'} \Lambda_{\tau'\tau}(p_i)], \quad (18)$$

$$\mathcal{C} = \sqrt{\frac{3}{2}} \left[\frac{2E_\Omega(\vec{q})}{m_\Omega} + \frac{2E_\Omega^2(\vec{q})}{m_\Omega^2} + \frac{E_\Omega^3(\vec{q})}{m_\Omega^3} + \frac{E_\Omega^4(\vec{q})}{m_\Omega^4} \right]^{-\frac{1}{2}}. \quad (19)$$

It is understood that the trace acts in spinor-space, while the Rarita-Schwinger spin sum, expressed in Euclidean space, is given by

$$\Lambda_{\sigma\tau}(p) \equiv \sum_s u_\sigma(p, s) \bar{u}_\tau(p, s) = -\frac{-i\not{p} + m_\Omega}{2m_\Omega} \left[\delta_{\sigma\tau} - \frac{\gamma_\sigma \gamma_\tau}{3} + \frac{2p_\sigma p_\tau}{3m_\Omega^2} - i \frac{p_\sigma \gamma_\tau - p_\tau \gamma_\sigma}{3m_\Omega} \right]. \quad (20)$$

The electromagnetic form factors are extracted by fitting $R_{\sigma\tau\mu}(\Gamma, \vec{q}, t)$ in the plateau region determined by $\Pi_{\sigma^\mu\tau}(\Gamma, \vec{q})$.

Since we are evaluating the correlator of Eq. (12) using sequential inversions through the sink [16], a separate set of inversions is necessary for every choice of vector and Dirac-indices. The total of 256 combinations arising from the vector indices of the Ω^- and the choice of Γ matrices, as can be inferred from Eq. (12), is beyond our computational resources, and hence we concentrate on a few carefully chosen combinations given below:

$$\begin{aligned} \Pi_\mu^{(1)}(\vec{q}) &= \sum_{j,k,l=1}^3 \epsilon_{jkl} \Pi_{j\mu k}(\Gamma^4, \vec{q}) \\ &= G_{M1} \frac{5i(E_\Omega + M_\Omega)\mathcal{C}}{18M_\Omega^2} [\delta_{1,\mu}(q_3 - q_2) + \delta_{2,\mu}(q_1 - q_3) + \delta_{3,\mu}(q_2 - q_1)], \end{aligned} \quad (21)$$

$$\begin{aligned} \Pi_\mu^{(2)}(\vec{q}) &= \sum_{k=1}^3 \Pi_{k\mu k}(\Gamma^4, \vec{q}) \\ &= -G_{E0} \frac{(E_\Omega + 2M_\Omega)\mathcal{C}}{3M_\Omega^2} [(M_\Omega + E_\Omega)\delta_{4,\mu} + iq_\mu(1 - \delta_{4,\mu})] \\ &\quad - G_{E2} \frac{(E_\Omega - M_\Omega)^2\mathcal{C}}{9M_\Omega^3} [(M_\Omega + E_\Omega)\delta_{4,\mu} + iq_\mu(1 - \delta_{4,\mu})], \end{aligned} \quad (22)$$

$$\begin{aligned}
\Pi_\mu^{(3)}(\vec{q}) &= \sum_{j,k,l=1}^3 \epsilon_{jkl} \Pi_{j\mu k}(\Gamma^j, \vec{q}) \\
&= G_{E2} \frac{-i\mathcal{C}}{3M_\Omega^2(E_\Omega + M_\Omega)} (q_1 q_2 + q_2 q_3 + q_3 q_1) \\
&\quad \times [(M_\Omega + E_\Omega) \delta_{4,\mu} + i q_\mu (1 - \delta_{4,\mu})] \\
&+ G_{M1} \frac{\mathcal{C}}{6M_\Omega^2(E_\Omega + M_\Omega)} \sum_{k=1}^3 \delta_{k,\mu} q_1 q_2 q_3 \left(2 - \frac{q_1 + q_2 + q_3 - q_k}{q_k} \right) \\
&+ G_{M3} \frac{\mathcal{C}}{30M_\Omega^3(E_\Omega + M_\Omega)} \sum_{k=1}^3 \delta_{k,\mu} \left[(16E_\Omega + 14M_\Omega) q_1 q_2 q_3 \right. \\
&\quad - 10M_\Omega (q_1 q_2 + q_2 q_3 + q_3 q_1) q_k \\
&\quad \left. - (8E_\Omega + 7M_\Omega) \frac{q_1 q_2 q_3}{q_k} (q_1 + q_2 + q_3 - q_k) \right],
\end{aligned} \tag{23}$$

where the kinematical factor \mathcal{C} is given in Eq. (19). As expected, current conservation $q_\mu \Pi_\mu = 0$ is manifest in the right hand side of the equations. From these expressions all the multipole form factors can be extracted. For instance Eq. (21) is proportional to G_{M1} , while Eq. (23) isolates G_{E2} for $\mu = 4$. Furthermore, these combinations are optimal in the sense that all momentum directions, each of which is statistically different, contributes to a given Q^2 -value. This symmetric construction yields a better estimator for the Ω^- -matrix elements than methods where only one momentum-vector is accessible.

In this paper, we consider only connected contributions to the three-point function. These are calculated by performing sequential inversions through the sink, which necessitates fixing the quantum numbers of the initial and final states as well as the time separation between the source and the sink. The optimal combinations given in Eq. (21) - Eq. (23), from which G_{E0} , G_{M1} and G_{E2} are determined, can be implemented by an appropriate sink construction which requires only one sequential inversion for each of the three types of combinations. No optimal sink is considered for the octupole magnetic form factor in this work. Although it can and has been extracted, the results exhibit large errors and are consistent with zero. We therefore refrain from presenting this specific form factor. The matrix element for all the different directions of \vec{q} and for all four directions μ of the current can then be computed yielding an over-constrained system of linear equations which can be solved for the form factors in the least squares sense. A singular value decomposition of the coefficient matrix is utilized to find the least squares solution. The statistical errors are found by a jack-knife procedure, which takes care of any possible autocorrelations between gauge configurations.

As already mentioned, the three-point function of the connected part is calculated by performing sequential inversions through the sink. This requires fixing the temporal source-sink separation. In order, to determine the smallest time separation that is still sufficiently large to damp excited state contributions, we perform the calculation at two values of the sink-source separation. We use $t_f/a = 8$ and $t_f/a = 10$ for the DWF configurations corresponding to the coarse lattice spacing $a = 0.114$ fm. We compare in Fig. 2 the results for the plateaus $\Pi_{\sigma\tau\mu}(\Gamma, \vec{q})$, for a few selected directions of the current and for low momentum \vec{q} values for these two sink-source time separations. As can be seen, the plateau values at $t_f/a = 10$ are consistent with the smaller time separation the latter exhibiting about half the statistical error. We therefore use $t_f/a = 8$ or $t_f = 0.91$ fm as source sink separation. For the fine DWF lattice the inversions were performed for $t_f/a = 12$, which corresponds to about $t_f = 1.008$ fm. Similarly for the hybrid scheme the time separation was taken to be at $t_f/a = 8$ or $t_f = 0.992$ fm.

III. RESULTS

We use the local electromagnetic current, $V^\mu = -\frac{1}{3} \bar{s} \gamma^\mu s$, which requires a renormalization factor Z_V to be included. The vector current renormalization constant is determined from the lattice calculation by the requirement that

$$Z_V G_{E0}(0) = -1, \tag{24}$$

where -1 is the charge of Ω^- . The values of Z_V extracted using Eq. (24) are given in Table III, where the errors shown are statistical. For the coarse lattice with DWF, the value of $Z_V = 0.7161(1)$ is calculated [17] from the pion decay constant. For the fine lattice Z_V was fixed using the nucleon electric form factor [6] with values $Z_V = 0.7468(39)$ at $m_\pi = 297$ MeV and $Z_V = 0.7479(22)$ at $m_\pi = 355$ MeV. For the mixed-action [18] with $m_\pi = 353$ MeV the value of the current renormalization constant $Z_V = 1.1169$ is obtained by dividing the unrenormalized isovector current

with the forward matrix element. These values differ by about 1%-2% with the ones found using Eq. (24). This discrepancy indicates systematic errors on the 2% level.

A. Electric charge form factor

Our results for the electric charge form factor, $G_{E0}(Q^2)$, are depicted in Fig. 3 for the fine and coarse lattice using DWF and for the mixed action. Results using the mixed action have consistently smaller values. This can be attributed either to cut-off effects or to a small dependence on the mass of the light sea quark mass. In order to check, we perform a calculation using DWF at $m_\pi = 355$ MeV on the fine lattice for the magnetic dipole form factor. This will be discussed in next section. In Fig. 3 we show fits to a dipole. As can be seen, the momentum dependence of this form factor is adequately described in all cases by a one-parameter dipole form

$$G_{E0}(Q^2) = -\frac{1}{\left(1 + \frac{Q^2}{\Lambda_{E0}^2}\right)^2}. \quad (25)$$

In the non-relativistic limit the slope of the above dipole form evaluated at momentum transfer $Q^2 = 0$, is related to the electric charge mean square radius by

$$\langle r_{E0}^2 \rangle = -\frac{6}{G_{E0}(0)} \left. \frac{d}{dQ^2} G_{E0}(Q^2) \right|_{Q^2=0}. \quad (26)$$

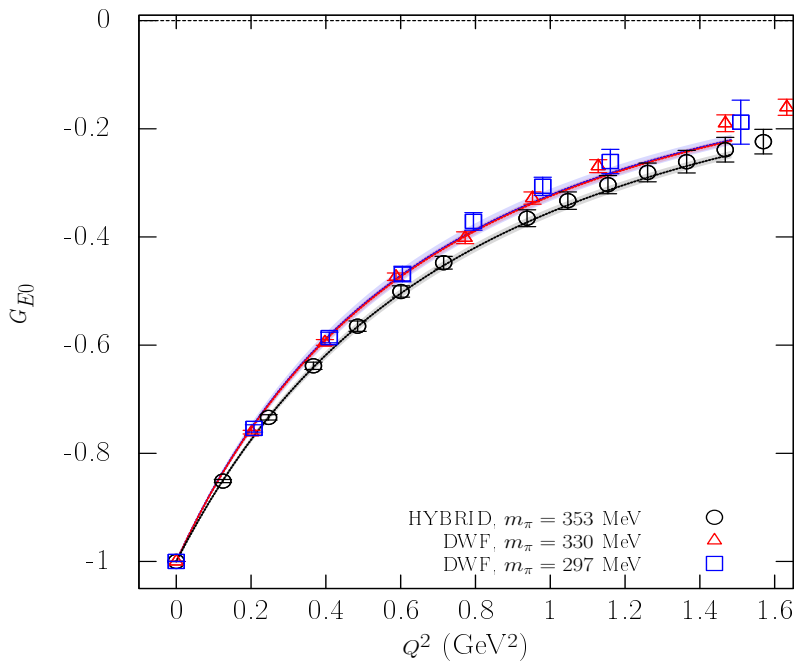


FIG. 3: The electric charge form factor $G_{E0}(Q^2)$ computed at $m_\pi = 330$ MeV and at $m_\pi = 297$ MeV. The lines describe the *dipole fits* given by Eq. (25), while the bands show the corresponding errors to the fits.

From the dipole fit to the coarse DWF lattice data we determine Λ_{E0} and obtain a value of $\langle r_{E0}^2 \rangle = 0.353(8) \text{ fm}^2$, while for the fine DWF lattice the corresponding value turns out to be $\langle r_{E0}^2 \rangle = 0.355(14) \text{ fm}^2$ ¹. These values are slightly greater in magnitude than the one reported in Ref. [19], which was obtained in a quenched lattice QCD calculation. The discrepancy may originate from unquenching effects or pronounced light quark mass dependence since the pion mass used in the quenched study of Ref. [19] is larger than what used here. The results for the $\langle r_{E0}^2 \rangle$ are given in Table III.

¹ Note the different sign as compared to Ref. [19] since we here divide by $G_E(0) = -1$.

B. Magnetic dipole form factor

In order to check for cut-off effects we perform a comparison between the hybrid results and results obtained at the same pion mass using DWF on our fine lattice. This comparison is shown in Fig. 4. The results using a hybrid action show a small deviation having a smaller slope as compared to the DWF results. This is the same behavior as was observed in the case of the electric form factor. Given the fact that the lattice spacing for the mixed action is the largest this points to cut-off effects. In Fig. 5 we show results obtained using DWF on the coarse and fine lattices, which are in agreement. This indicates that for these lattice spacings cut-off effects are small.

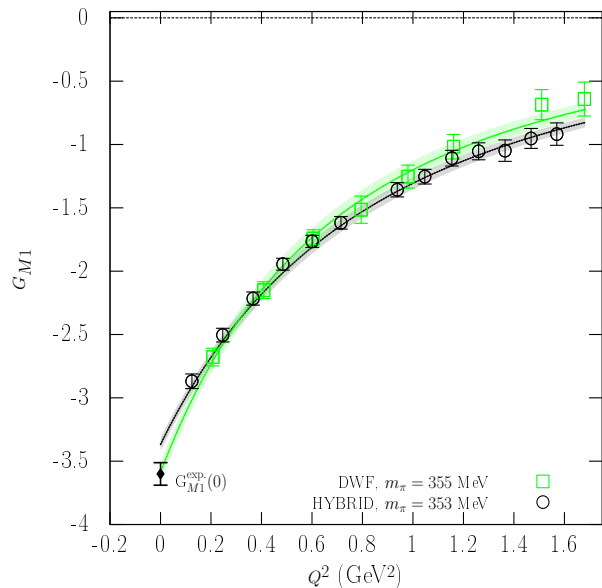


FIG. 4: The magnetic form factor $G_{M1}(Q^2)$ comparing the results from the mixed action approach and the DWF lattice at $m_\pi \sim 350$ MeV.

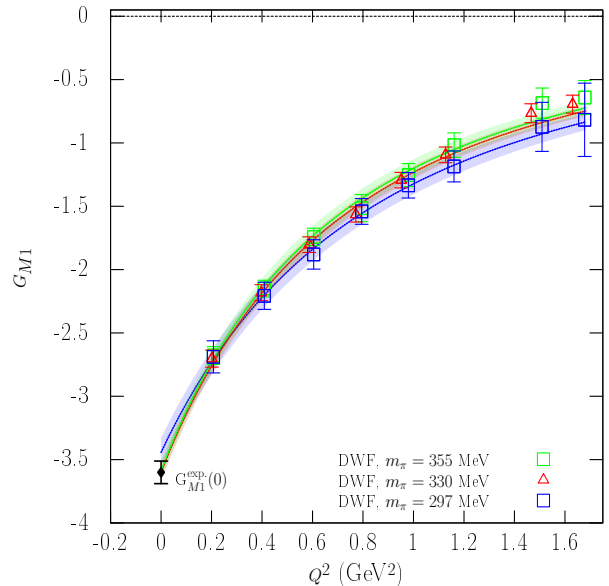


FIG. 5: The magnetic dipole form factor, G_{M1} , using DWF at $m_\pi = 353$ MeV, $m_\pi = 330$ MeV and $m_\pi = 297$ MeV. These results are shown along with the *dipole fit* as given in Eq. (28). The datum for the magnetic dipole form factor at $Q^2 = 0$ GeV², $G_{M1}^{\text{exp}}(0) = -3.60(8)$, is also included.

The Q^2 -dependence of the form factors, as in the case of G_{E0} , can be described by a dipole form as can be seen in Figs. 4 and 5. Fitting to the two-parameter exponential, dipole and tripole forms

$$G_{M1}(Q^2) = G_0 \exp\left(-\frac{Q^2}{\Lambda_{M1}^2}\right), \quad (27)$$

$$G_{M1}(Q^2) = \frac{G_0}{\left(1 + \frac{Q^2}{\Lambda_{M1}^2}\right)^2}, \quad (28)$$

$$G_{M1}(Q^2) = \frac{G_0}{\left(1 + \frac{Q^2}{\Lambda_{M1}^2}\right)^3}, \quad (29)$$

we can obtain a value for the anomalous magnetic moment of the Ω^- .

By utilizing the fit parameter, $G_0 \equiv G_{M1}(0)$, and the lattice computed Ω^- mass from Table II, we can evaluate the magnetic moment in nuclear magnetons, via the relation

$$\mu_{\Omega^-} = G_0 \left(\frac{e}{2m_\Omega}\right) = G_0 \left(\frac{m_N}{m_\Omega}\right) \mu_N. \quad (30)$$

Our value of μ_{Ω^-} in nuclear magnetons μ_N is given in Table III. The values obtained are in accord with two other recent lattice calculations [19, 20]. The calculation in Ref. [19] is similar to ours in the sense that the three-point correlation function is also calculated, but the evaluation is carried out in the quenched theory and only at one value of Q^2 . In Ref. [20] a background field method was employed, where energy shifts were computed using $N_F = 2 + 1$ clover fermions at pion mass of 366 MeV on an anisotropic lattice.

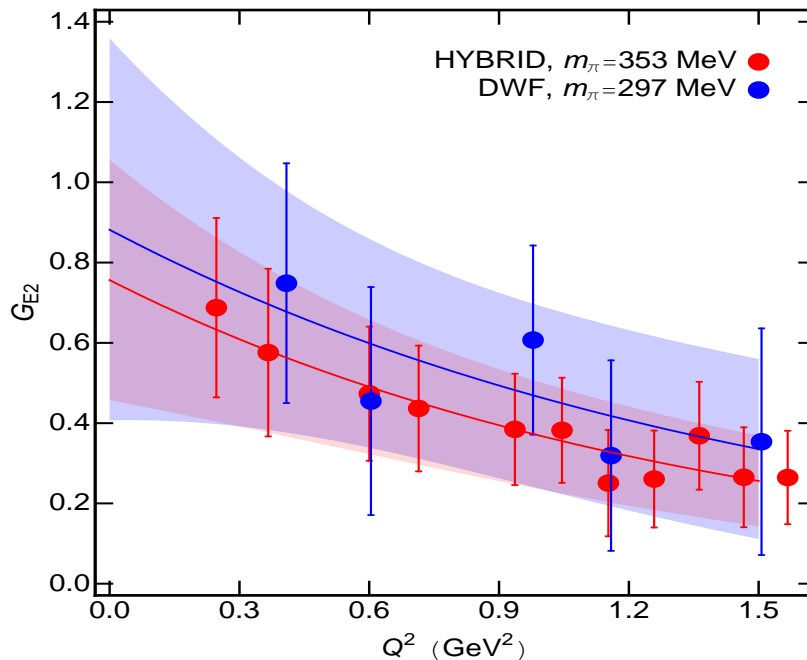


FIG. 6: The subdominant electric quadrupole form factor $G_{E2}(Q^2)$ for DWF using the fine lattice at $m_\pi = 297$ MeV, and using the hybrid action at $m_\pi = 353$ MeV. The extrapolated values at $Q^2 = 0$ are also depicted. The two results, apart from being consistent within errors indicate a non-zero deformation for the Ω^- baryon.

type of fit	Λ_{E0} [GeV]	$\chi^2_{E0}/\text{d.o.f}$	G_0	Λ_{M1} [GeV]	$\chi^2_{M1}/\text{d.o.f}$
$N_F = 2 + 1$ DWF ($24^3 \times 64$), $N_{\text{confs}} = 200$					
exponential			-3.264(89)	1.016(27)	0.225
dipole	1.151(13)	1.500	-3.601(109)	1.187(41)	0.860
tripole			-3.478(101)	1.555(49)	0.435
$N_F = 2 + 1$ DWF ($32^3 \times 64$), $N_{\text{confs}} = 105$; $m_\pi = 355$ MeV					
exponential			-3.246(96)	0.996(43)	0.159
dipole			-3.557(130)	1.171(63)	0.440
tripole			-3.443(116)	1.530(76)	0.240
$N_F = 2 + 1$ DWF ($32^3 \times 64$), $N_{\text{confs}} = 120$; $m_\pi = 297$ MeV					
exponential			-3.199(155)	1.061(48)	0.080
dipole	1.146(23)	0.887	-3.443(173)	1.277(68)	0.064
tripole			-3.355(165)	1.656(83)	0.040
Hybrid ($28^3 \times 64$), $N_{\text{confs}} = 120$					
exponential			-3.154(69)	1.064(30)	1.147
dipole	1.213(17)	0.168	-3.368(80)	1.285(44)	0.163
tripole			-3.293(76)	1.662(54)	0.053

TABLE II: The fit parameters for the exponential, dipole and tripole forms extracted from the lattice data. For the fine lattice with $m_\pi = 355$ MeV DWF we have only performed inversions for the source type associated with the dominant magnetic dipole form factor $G_{M1}(Q^2)$ (see Eq. (21)).

C. Electric quadrupole form factor

From the perspective of hadron structure, the extraction of the electric quadrupole form factor is of special interest since it can be used to provide valuable information regarding the deformation of a hadron. In this work we extract for the first time in unquenched QCD the subdominant G_{E2} form factor for the Ω^- baryon, to sufficient accuracy to exclude zero values. This has been achieved by utilizing two different lattices: namely, the fine DWF lattice and the MILC lattice at lattice spacings of $a = 0.084$ fm and $a = 0.124$ fm respectively. We note that for the coarse DWF lattice the results for G_{E2} are too noisy to exclude a zero value and we therefore do not present them here. The lattice

	lattice	m_π	Z_V	μ_{Ω^-}	$\langle r_{M1}^2 \rangle$	$\langle r_{E0}^2 \rangle$	$G_{E2}(0)$	$Q_{\frac{3}{2}}^\Omega$
	$[L_s^3 \times L_t]$	[GeV]		$[\mu_N]$	$[\text{fm}^2]$	$[\text{fm}^2]$		$[e/m_\Omega^2]$
This work	HYB: $28^3 \times 64$	0.353	1.121(2)	-1.775(52)	0.283(20)	0.338(9)	0.838(19)	-1.366(222)
	DWF: $24^3 \times 64$	0.330	0.727(1)	-1.904(71)	0.332(23)	0.353(8)	—	—
	DWF: $32^3 \times 64$	0.355	0.7479(22)	-1.868(78)	0.341(37)	—	—	—
	DWF: $32^3 \times 64$ extrapolated	0.297	0.7543(4)	-1.835(94)	0.286(31)	0.355(14)	0.959(41)	-1.892(204)
Ref. [19]	$20^3 \times 40$	0.697	1	-1.697(65)	—	0.307(15)	—	—
Ref. [20]	$24^3 \times 128$	0.366	—	-1.93(8)	—	—	—	—
Ref. [1]	—	—	—	-2.02(5)	—	—	—	—

TABLE III: The magnetic moment μ_{Ω^-} , the electric charge and magnetic radii and the electric quadrupole moment $Q_{\frac{3}{2}}^\Omega$ as extracted using Eq. (31). The values of μ_{Ω^-} , $\langle r_{M1}^2 \rangle$, $\langle r_{E0}^2 \rangle$ and $Q_{\frac{3}{2}}^\Omega$ shown above arise from the dipole fit form. Note that $\langle r_{M1}^2 \rangle = -\frac{6}{G_{M1}(0)} \frac{dG_{M1}(Q^2)}{dQ^2} \Big|_{Q^2=0}$.

results for G_{E2} are depicted in Fig. 6. The value of the quadrupole electric form factor $G_{E2}(Q^2)$ at $Q^2 = 0$ using the exponential form to fit the lattice results is 0.756(298) for the hybrid action and 0.882(475) for the fine DWF lattice. From these results it is readily deduced that the shape of the Ω^- hyperon must deviate from the spherical one.

The electric quadrupole moment determined from the fits as $Q_\Omega = G_{E2}(0) \frac{e}{m_\Omega^2}$ can be related to the transverse charge density in the infinite momentum frame. For instance, the transverse charge density defined in the light-front for spin projection 3/2, is given by [21, 22]

$$Q_{\frac{3}{2}}^\Omega = \frac{1}{2} \left\{ 2[G_{M1}(0) - 3e_\Omega] + [G_{E2}(0) + 3e_\Omega] \right\} \left(\frac{e}{m_\Omega^2} \right). \quad (31)$$

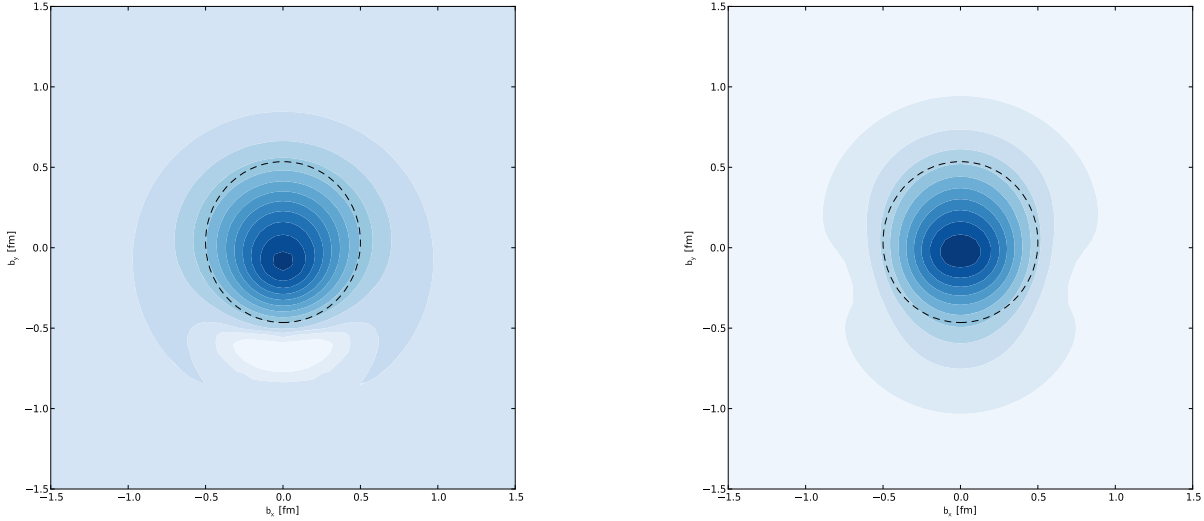


FIG. 7: Transverse charge densities in the Ω^- with polarization along the x-axis. Left: $\rho_{T_{3/2}}^\Omega(\vec{b})$. Right: $\rho_{T_{1/2}}^\Omega(\vec{b})$. A circle of radius 0.5 fm is drawn in order to clearly demonstrate the deformation. For the evaluation of the densities we used the dipole parametrization of the form factors.

We note that for a spin- $\frac{3}{2}$ particle without internal structure, for which $G_{M1}(0) = 3e_\Omega$ and $G_{E2}(0) = -3e_\Omega$ [21, 22], the quadrupole moment of the transverse charge densities vanishes. We calculate this quantity by using a fit to the electric quadrupole to obtain the value at $Q^2 = 0$. The results obtained are shown in Table III and plotted in Fig. 10 for the dipole fitting Ansatz. Both of the two values are negative and consistent within statistical errors. Therefore, they suggest that the quark charge distribution in the Ω^- must be deformed. In order to investigate the deformation in more detail we construct the transverse charge density in the infinite momentum frame, following Refs. [21, 22]. Considering the spin of the Ω along the x-axis and states of transverse spin $s_\perp = 3/2$ and $s_\perp = 1/2$ we obtain the transverse charge densities $\rho_{T_{3/2}}^\Omega(\vec{b})$ and $\rho_{T_{1/2}}^\Omega(\vec{b})$ in term of the two-dimensional impact parameter \vec{b} . In Fig. 7 we compare $\rho_{T_{3/2}}^\Omega(\vec{b})$ and $\rho_{T_{1/2}}^\Omega(\vec{b})$. As can be seen, in a state of transverse spin projection $s_\perp = 3/2$ the Ω^- shows a

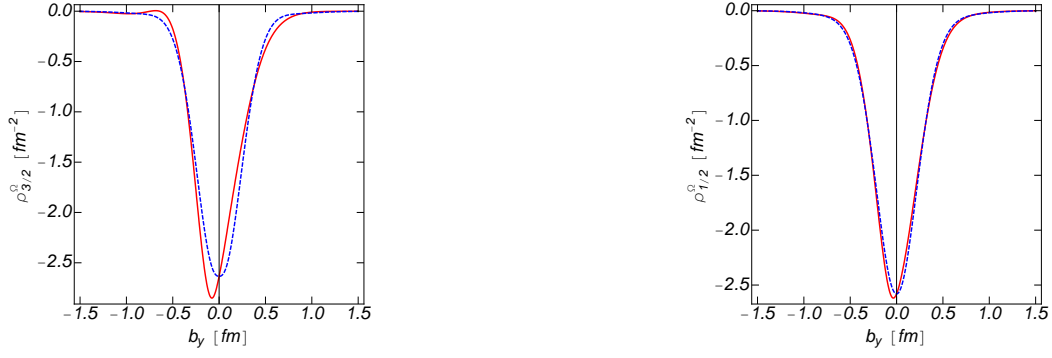


FIG. 8: Comparison of the transverse charge densities $\rho_{T_{3/2}}^{\Omega}(\vec{b})$ (left) and $\rho_{T_{1/2}}^{\Omega}(\vec{b})$ (right) along the y-axis to the monopole-field (symmetric) shown by the dashed line.

small elongation along the spin axis (prolate)². This elongation is less as compared to that seen for the Δ^+ . As in the case of the Δ^+ , in a state of transverse spin projection $s_{\perp} = 1/2$ the Ω^- is elongated along the axis perpendicular to the spin.

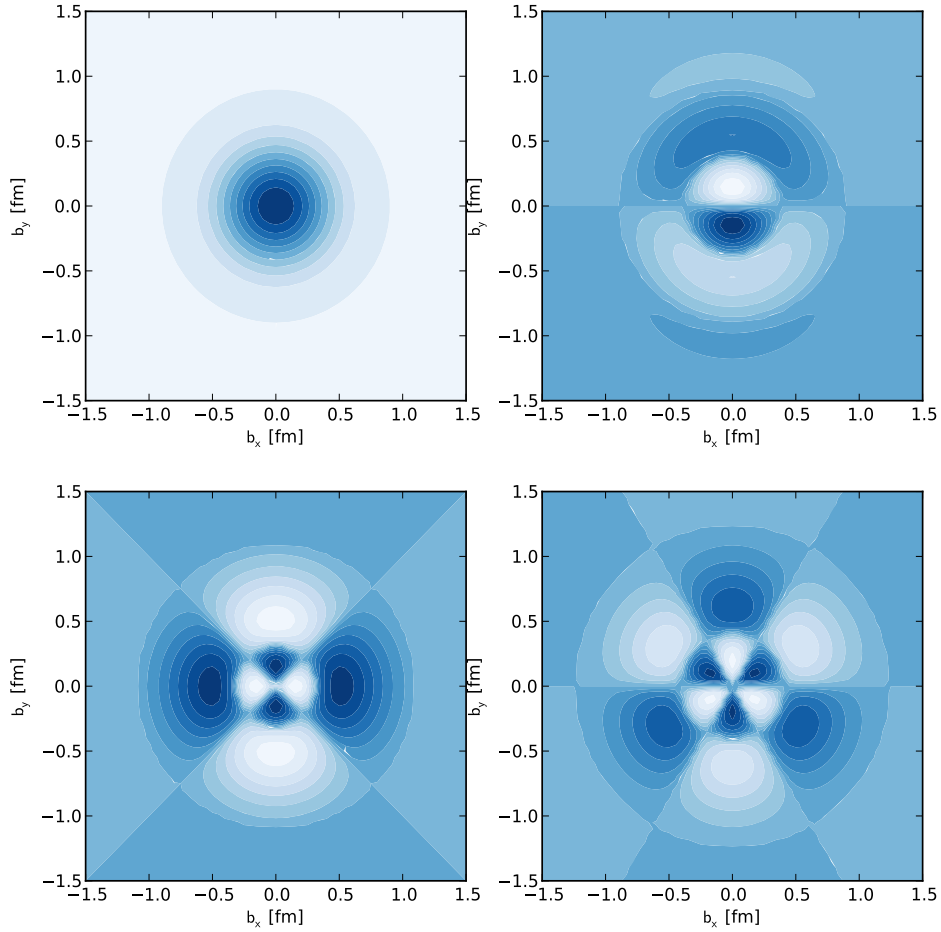


FIG. 9: The individual multipoles for the transverse charge density $\rho_{T_{3/2}}^{\Omega}(\vec{b})$ in the Ω^- with polarization along the x-axis. Upper left: monopole-field. Upper right: dipole-field. Lower left: quadrupole-field. Lower right: Octupole-field

² Note that this is consistent with the negative sign of $Q_{3/2}$ since the Ω^- is negatively charged and have included its charge in the electromagnetic current

In Fig. 8 we show the profile of the transverse densities compared to the monopole field that is symmetric. In Fig. 9 we show the individual multipole fields for the state with transverse spin $s_{\perp} = 3/2$.

D. Extrapolation to the physical point

In this section we examine the sea quark dependence of the magnetic moment, radii and the quadrupole moment. They are extracted by fitting the Q^2 -dependence of the form factors to a dipole form. As can be seen from Fig. 10 the sea quark mass dependence is consistent with a constant for all quantities confirming that sea quark effects are small. In particular, the value of the magnetic form factor at $Q^2 = 0$ is consistent with experiment. On the other hand extrapolating the magnetic moment we obtain the value given in Table III. This is 5% smaller than experiment which is to be expected given the larger value of the strange quark mass. The reason is that the mass of the Ω^- is 5% larger than experiment and this will affect the value of the magnetic moment when we convert to nuclear magnetons. In the fits for the magnetic moment and radii we did not include the results obtained in the hybrid action because of the small finite a effects observed. Given the large statistical errors on quadrupole moment such small finite- a effects are negligible and therefore, in this case, we include the result using the hybrid action to obtain the extract the value at the physical point. In Table III we give the values that we find at the physical point for the radii and the dipole and quadrupole moments of the transverse charge density obtained from Eq. (31).

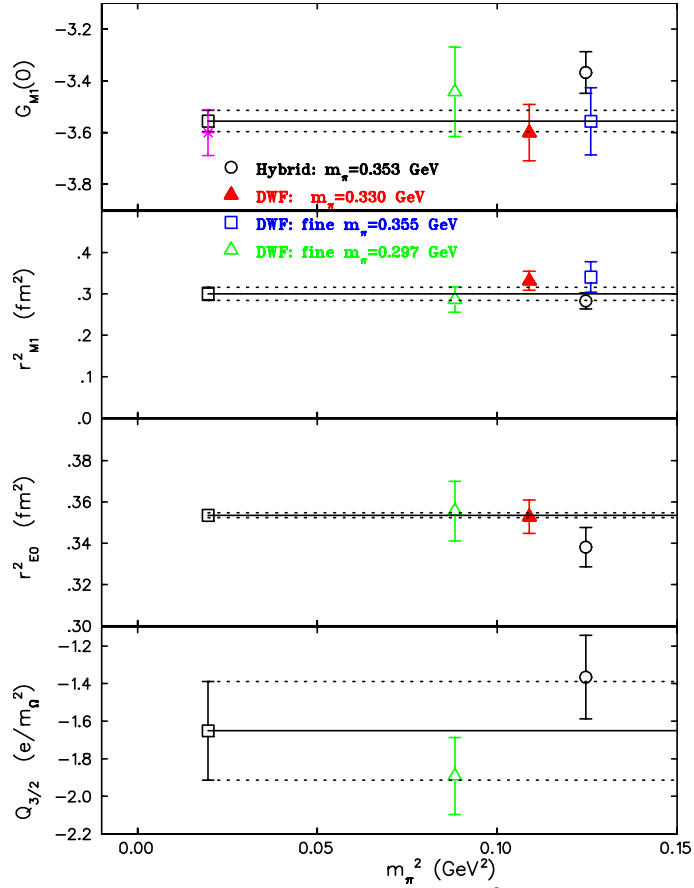


FIG. 10: From top to bottom we show $G_{M1}(0)$, the magnetic radius (r_{M1}^2), the electric radius (r_{E0}^2) and the quadrupole moment extracted from Eq. (31) as a function of m_{π}^2 extracted from dipole fits. The point shown by the filled square is the value extracted from the fit at the physical pion mass. In all cases except for the quadrupole moment the results using the hybrid action are excluded from the fit.

IV. CONCLUSIONS

By utilizing properly constructed sequential sources the dominant Ω^- electromagnetic form factors G_{E0} and G_{M1} are calculated with good accuracy using dynamical domain-wall fermion configurations as well as a hybrid action.

In addition, we extract the magnetic moment of the Ω^- by fitting the magnetic dipole form factor G_{M1} to a two-parameter dipole form. We find a value that is within errors to the experimentally measured value [1]. The electric charge and magnetic radii ($\langle r_{E0}^2 \rangle$ and $\langle r_{M1}^2 \rangle$) are computed and like the magnetic dipole moment they do not show sea quark dependence in the range of masses studied in this work.

Finally, the subdominant electric quadrupole form factor G_{E2} is computed for the first time in an unquenched lattice calculation to sufficient accuracy to exclude a zero value. This has been accomplished by constructing an appropriate sink that isolates it from the two dominant form factors. We find consistent results with DWF and using a hybrid action. The positive non-zero values of G_{E2} at $Q^2 = 0$ suggest that the structure of the Ω^- baryon is non-spherical. In the light-front frame we find that the quark charge density in a Ω^- for a state of transverse spin projection $+3/2$ shows an elongation along the axis of the spin (prolate deformation). As compared to the Δ^+ in the same state the amount of deformation seen in the Ω^- is smaller.

Acknowledgments

This research was partly supported by the Cyprus Research Promotion Foundation (R.P.F) under contracts IIENEK/ENIEX/0505-39 and EPYAN/0506/08 and by the U.S. Department of Energy under Grant DE-FG02-94ER-40818. The authors would also like to acknowledge the use of dynamical domain wall fermions configurations provided by the RBC-UKQCD collaborations and the use of Chroma software [23]. Part of the computational resources required for these calculations were provided by the Jülich Supercomputing Center at Research Center Jülich.

-
- [1] C. Amsler *et al.* (Particle Data Group), PL **B667** (2008) 1.
 - [2] C. Alexandrou *et al.*, Phys. Rev. D **79** (2009) 014507.
 - [3] K. Orginos, D. Toussaint and R. L. Sugar [MILC Collaboration], Phys. Rev. D **60**, 054503 (1999) [arXiv:hep-lat/9903032].
 - [4] S. Nozawa and D. B. Leinweber, Phys. Rev. D **42** (1990) 3567.
 - [5] C. Allton *et al.* [RBC-UKQCD Collaboration], Phys. Rev. D **78** (2008) 114509.
 - [6] S. N. Syritsyn *et al.*, Phys. Rev. D **81**, 034507 (2010) [arXiv:0907.4194 [hep-lat]].
 - [7] C. W. Bernard *et al.*, Phys. Rev. D **64**, 054506 (2001) [arXiv:hep-lat/0104002].
 - [8] C. Aubin *et al.* [HPQCD Collaboration and MILC Collaboration and UKQCD Collaboration], Phys. Rev. D **70**, 031504 (2004) [arXiv:hep-lat/0405022].
 - [9] A. Walker-Loud *et al.*, Phys. Rev. D **79**, 054502 (2009) [arXiv:0806.4549 [hep-lat]].
 - [10] D. B. Renner *et al.* [LHP Collaboration], Nucl. Phys. Proc. Suppl. **140**, 255 (2005) [arXiv:hep-lat/0409130].
 - [11] Ph. Hagler *et al.* [LHPC Collaborations], Phys. Rev. D **77**, 094502 (2008) [arXiv:0705.4295 [hep-lat]].
 - [12] Y. Aoki *et al.*, arXiv:1003.3387 [hep-lat].
 - [13] C. Alexandrou, S. Gusken, F. Jegerlehner, K. Schilling and R. Sommer, Nucl. Phys. B **414** (1994) 815.
 - [14] M. Albanese *et al.* (APE Collaboration) Phys. Lett. B **192** (1987) 163.
 - [15] I. Montvay and G. Munster, *Cambridge, UK: Univ. Pr. (1994) 491 p. (Cambridge monographs on mathematical physics)*
 - [16] D. Dolgov *et al.* [LHPC collaboration and TXL Collaboration], Phys. Rev. D **66**, 034506 (2002) [arXiv:hep-lat/0201021].
 - [17] Y. Aoki *et al.*, Phys. Rev. D **78** (2008) 054510.
 - [18] J. D. Bratt *et al.* [LHPC Collaboration], arXiv:1001.3620 [hep-lat].
 - [19] S. Boinepalli, D. B. Leinweber, P. J. Moran, A. G. Williams, J. M. Zanotti and J. B. Zhang, Phys. Rev. D **80**, 054505 (2009), arXiv:0902.4046 [hep-lat].
 - [20] C. Aubin, K. Orginos, V. Pascalutsa and M. Vanderhaeghen, Phys. Rev. D **79**, 051502 (2009), arXiv:0811.2440 [hep-lat].
 - [21] C. Alexandrou *et al.*, Nucl. Phys. A **825** (2009) 115.
 - [22] C. Alexandrou *et al.*, PoS C **D09**, 092 (2009) [arXiv:0910.3315 [hep-lat]].
 - [23] R. G. Edwards and B. Joo [SciDAC Collaboration and LHPC Collaboration and UKQCD Collaboration], Nucl. Phys. Proc. Suppl. **140**, 832 (2005) [arXiv:hep-lat/0409003].